Research in Astron. Astrophys. Vol.0 (200x) No.0, 000–000
http://www.raa-journal.org *http://www.iop.org/journals/raa*

***R**esearch in*
***A**stronomy and*
***A**strophysics*

The peculiar in-plane velocities in the outer disc of the Milky Way

Hai-Jun Tian[1,2], Chao Liu[3], Jun-Chen Wan[3], You-Gang Wang[4], Qiao Wang[4], Li-Cai Deng[3], Zi-Huang Cao[3], Yong-Hui Hou[5], Yue-Fei Wang[5], Yue Wu[3] and Yong-Heng Zhao[3]

[1] China Three Gorges University, Yichang 443002, China; *hjtian@lamost.org*
[2] Max Planck Institute for Astronomy, Königstuhl 17, D-69117 Heidelberg, Germany;
[3] Key Lab for Optical Astronomy, National Astronomical Observatories, Chinese Academy of Sciences, Beijing 100012, China;*liuchao@nao.cas.cn*
[4] Key Laboratory of Computational Astrophysics, National Astronomical Observatories, Chinese Academy of Sciences, Beijing, 100012 China;*wangyg@bao.ac.cn*
[5] Nanjing Institute of Astronomical Optics & Technology, National Astronomical Observatories, Chinese Academy of Sciences, Nanjing 210042, China;

Received 2017 June 9; accepted 2017 July 26

Abstract We present the peculiar in-plane velocities derived from the LAMOST red clump stars, which are purified and separated by a novel approach into two groups with different ages. The samples are mostly contributed around the Galactic anti-centre direction such that we are able to map the radial profiles of the radial and azimuthal velocities in the outer disc. From the variations of the in-plane velocities with the Galactocentric radius for the younger and older populations, we find that both radial and azimuthal velocities are not axisymmetric at $8 < R < 14$ kpc. The two red clump populations show that the mean radial velocity is negative within $R \sim 9$ kpc and positive beyond. This is likely because of the perturbation induced by the rotating bar. The cross-zero radius, $R \sim 9$ kpc, essentially indicates the rough location of the outer Lindblad resonance (OLR) radius. Given the circular speed of 238 km s^{-1}, then the pattern speed of the bar can be approximated as 45 km $\mathrm{s}^{-1}\mathrm{kpc}^{-1}$. The young red clump stars show larger mean radial velocity than the old population by about 3 km s^{-1} between $R \sim 9$ and 12 kpc. This is possibly because the younger population is more sensitive to the perturbation than the older one. The radial profiles of the mean azimuthal velocity for the two populations show an interesting U-shape, i.e. at $R < 10.5$ kpc, the azimuthal velocity declines with R by about 10 km s^{-1}, while at $R > 10.5$ it increases with R to 240-245 km s^{-1}. It is not clear why the mean azimuthal velocity shows the U-shape along the Galactic anti-centre direction. Meanwhile, the azimuthal velocity for the younger population is slightly larger than the older one and the difference moderately declines with R. Beyond $R \sim 12$ kpc, the azimuthal velocities for the two populations are indistinguishable.

Key words: Galaxy: disc — Galaxy: structure — Galaxy: kinematics and dynamics — Galaxy: stellar content — stars: kinematics and dynamics

1 INTRODUCTION

In recent years, the Galactic disc is found not symmetric in both the stellar density and kinematics. Widrow et al. (2012) claimed that the vertical stellar density shows small-amplitude but significant oscillation in both the north and south of the Galactic mid-plane. Xu et al. (2015) discovered the wave-like

ring from the stellar count in the Galactic outer disc. Siebert et al. (2011a) found from the RAVE survey data (Siebert et al., 2011b) that the radial velocity in the solar neighbourhood is not symmetric, the stars show bulk motion of about 7 km s^{-1} toward the inner Galaxy. Bond et al. (2010) also confirmed this from the SDSS survey data. Carlin et al. (2013), Williams et al. (2013), and Sun et al. (2015) demonstrated that the asymmetric motion is not only in radial, but also in vertical direction. Tian et al. (2015) showed that the asymmetric motion may be related to the age of the stars, i.e., the younger populations show larger peculiar velocity in both radial and vertical directions than the old populations. Bovy et al. (2015) studied the power spectrum of the velocity map in the X–Y plane with the APOGEE (Alam et al., 2015) red clump stars and argued that the velocity oscillation with a broad peak at the wave number of 0.2–0.9 kpc^{-1} is likely due to the Galactic central bar.

Although some works attribute the asymmetric stellar density and the oscillated velocity to the perturbation of minor mergers (Gómez et al. , 2013), many other theoretical works associated the peculiar velocity with either the spiral structures or the rotating bar located in the central region of the Galaxy. Siebert et al. (2012), who used a simplified model of the perturbation from the spiral density wave, and Faure et al. (2014), who ran N-body simulations with spiral arms, attributed the radial asymmetric motion to the perturbation induced by the spiral structures. Debattista (2014) found from the N-body simulations that the (strong) spiral structures can also induce vertical oscillation near the disc mid-plane. Recently, Grand et al. (2015) applied the power spectrum approach to the N-body simulation data and found that the bar with transient co-rotating spiral structures can produce similar features found in Bovy et al. (2015).

For a disc with a rotating bar in the central region, the originally circular closed orbits in axisymmetric gravitational potentials would become elliptical due to the perturbation of the rotating weak bar potential. Contopoulos & Papayannopoulos (1980) derived that the radius of the closed loop orbit is a function of the azimuth angle (also see Eqs (3.148a,b) in Binney & Tremaine, 2008) and displayed that, in the rotating frame, the major-axes of the closed loop orbits change their direction at various radii: inside Inner Lindblad Resonance radius (ILR) the major axes of the closed loop orbits are aligned with the minor-axis of the bar; between ILR and Corotation Resonance radius (CR) they are aligned with the major-axis of the bar; between CR and Outer Lindblad Resonance radius (OLR) they are aligned with the minor-axis again; and beyond OLR they are aligned back with the major-axis of the bar. The reshaping of the orbits at different radii may leads to non-zero and oscillated mean in-plane velocities in the disc.

In this paper, we investigate the peculiar in-plane velocities from Galactocentric radius of $R \sim 7$ to 14 kpc in the Galactic disc using the red clump stars mostly distributed in the Galactic anti-center region from the LAMOST survey (Cui et al. , 2012; Zhao et al., 2012).

The paper is organized as follows. In Section 2, we describe how to refine the red clump stars from the LAMOST catalog and separate them into young and old populations. In Sections 3, we discuss the approach to derive the mean in-plane velocity based on the velocity de-projection technique. In Section 4, we demonstrate our results of the peculiar in-plane velocities, which show oscillations in both the radial and azimuthal components. In Section 5, we discuss the possible mechanisms which induce these peculiar velocities. Finally, we draw brief conclusions in Section 6.

2 DATA

The Large Aperture Multi-Object fiber Spectroscopic Telescope (LAMOST, also called Guoshoujing telescope), is a quasi-meridian reflecting Schmidt telescope with the effective aperture of about 4 meters. Totally 4000 fibers, which are capable of obtaining the similar number of low resolution spectra (R$\sim$ 1800) covering from 380 to 900 nm simultaneously, are installed on its 5° focal plane (Cui et al. , 2012; Zhao et al., 2012). In the 5-year survey plan, it will obtain a few millions of stellar spectra in about 20,000 square degrees in the northern sky (Deng et al. , 2012). A large fraction of the survey footprints cover the Galactic anti-center region due to the special site situations (Yao et al., 2012).

As December 2015, LAMOST has delivered its third data release (DR3), containing about 5.7 million stellar spectra. Among them, the LAMOST pipeline has provided stellar astrophysical parameters

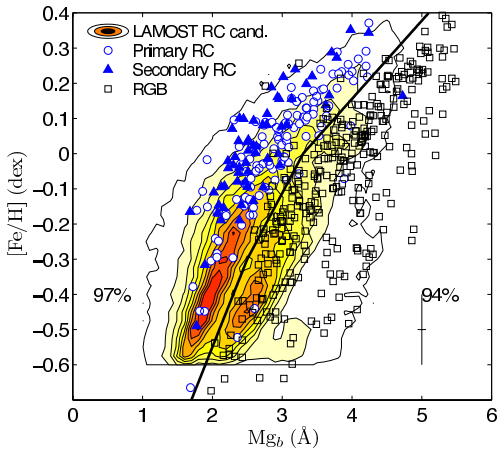

Fig. 1 The distribution of the RC candidate stars from Wan et al. (2015) in the [Fe/H]-Mg$_b$ plane. The contours show the number density of the LAMOST RC candidates. The black rectangles, blue circles, and blue filled triangles are the RGB stars, the primary, and the secondary RC stars identified by Stello et al. (2013), respectively. The black solid line indicates the empirical separation between the RGB (below) and the RC (above) stars.

(effective temperature, surface gravity, and metallicity) as well as line-of-sight velocities for about 3 millions FGK type stars (Wu et al., 2014). Most of the spectra have well measured line indices (Liu et al., 2015a). Based on the line indices and applying the classification approach developed by Liu et al. (2014b), about 700 thousands K giant stars are identified from the LAMOST DR3 catalog. Liu et al. (2015b) have improved the surface gravity (log$g$) estimation to the uncertainty of ~ 0.1 dex for the metal-rich giant stars. Wan et al. (2015) subsequently identified about a hundred thousands of red clump (RC) star candidates based on the empirical distribution model in the $T_{\rm eff}$–log$g$–[Fe/H] space. Not only the primary RC stars, which are usually considered as standard candles, but also the secondary RC stars, which are more massive and young, are recognized in Wan et al. (2015). The distances to both types of RC stars are estimated by these authors using isochrone fitting with accuracy of $\sim 10\%$.

2.1 Removing the RGB contaminations

The technique used in Wan et al. (2015) is based on statistics, i.e., for each star, the method can only give the probability to be a RC star. Consequently, a small fraction of red giant branch (RGB) stars are mixed in the RC candidates. In order to remove these contaminations, we apply another technique mentioned in the Appendix of Liu et al. (2014b) to further disentangle the RGB stars from the RC candidates. We map the RC candidates to the [Fe/H] vs. Mg$_b$ plane, where Mg$_b$ is the Lick index for the spectral line of Mg I located around 5184 Å based on Worthey et al. (1994), in Figure 1. It is obviously seen that the density map of the RC candidates in [Fe/H] vs. Mg$_b$ plane shows clear bimodality with a elongated gap from [Fe/H]=-0.6 dex and Mg$_b\sim$ 2 Å to [Fe/H]~ -0.1 dex and Mg$_b\sim$ 2.5 Å. Because the RC stars are always warmer than the RGB stars given the same metallicity and surface gravity, they show relatively smaller values of Mg$_b$ than the RGB stars with same [Fe/H] and log$g$. On the other hand, log$g$ of the RC stars should be smaller than that of the RGB stars with same metallicity and effective temperature. The smaller log$g$ also leads to smaller value of Mg$_b$. Combining the two trends together, given a metallicity, the RC stars always locate at the side with smaller Mg$_b$ than the RGB stars.

Therefore, the clump with smaller Mg$_b$ should be mostly contributed by the RC stars, while the other clump with larger Mg$_b$ should be contributed by the RGB stars. For the stars with [Fe/H]> -0.1, the separation between the RC and RGB stars is not quite clear. We then superpose the common stars

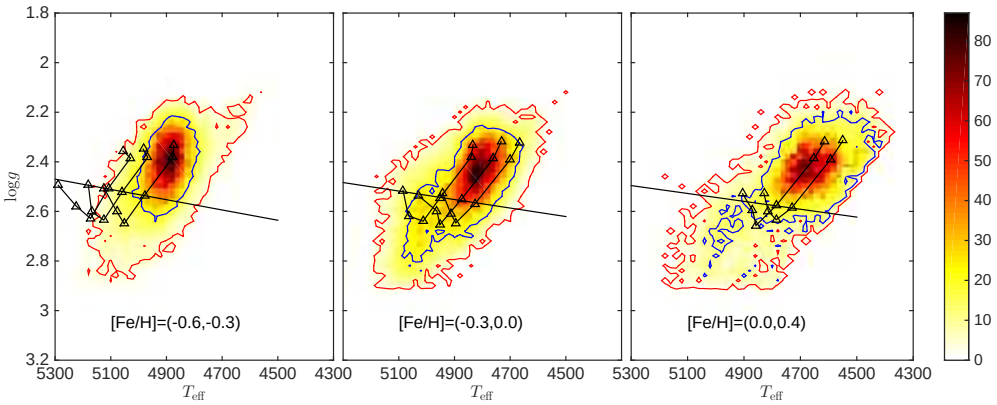

Fig. 2 The separation of the young and old RC stars in three [Fe/H] bins, -0.6<[Fe/H]<-0.3 (left panel), -0.3<[Fe/H]<0 (middle panel), and 0<[Fe/H]<0.4 (right panel). The black triangles are the isochrones for the helium core burning stars from Bressan et al. (2012). From the left to the right in the left panel, the isochrones are at [Fe/H]=-0.6, -0.5, and -0.4. For each isochrone, the triangles represent for 0.2, 0.5, 1.0, 2.0, 3.0, and 5.0 Gyr from left to top-right. In the middle panel, the isochrone tracks are at [Fe/H]=-0.3, -0.2, and -0.1 from left to right, respectively. In the right panels, the isochrones are at [Fe/H]=0.1 and 0.3 from left to right, respectively. The straight lines are the best fit of the points of isochrones with age=2 Gyr in different ranges of [Fe/H]. Below the lines are the isochrone-based young population with age$<$ 2 Gyr and above are the old population with age$>$ 2 Gyr. The color codes the stellar density.

between the LAMOST and Stello et al. (2013), who classified the RGB, primary and secondary RC stars from the seismic features. The RC stars (blue hollow circles for the primary RC stars and the blue filled triangles for the secondary RC stars) and the RGB stars (represented with the black hollow rectangles) from Stello et al. (2013) are well separated in the [Fe/H]–Mg$_b$ plane. Then, we are able to extend the separation between RGB and RC stars over the broad range of metallicity using the empirical separation line from (Mg$_b$, [Fe/H])=(2.1, -0.5), (2.5, -0.3), through (3.3, 0.0) to (5.0 Å, 0.38 dex) (the thick black line).

With the empirical separation, 97% seismic-identified RC stars are identified as RC stars and 94% seismic-identified RGB stars are classified as RGB stars. The empirical identification of the RC stars shown in Figure 1 can reduce the contamination of the RGB stars by only about 2%, according to the data from Stello et al. (2013).

2.2 The young and old RC populations

The primary RC stars are those in the helium core burning stage which had the degenerate helium core in late RGB stage and have experienced the helium flash. On the other hand, the secondary RC stars have initial stellar mass larger than the critical mass of helium flash (around 2M$_\odot$) and thus ignite the helium core before the core becomes electronic degenerate. Because the different evolutionary tracks, the positions for the two types of stars in the Hertzprung–Russell diagram (or equivalently, the $T_{\rm eff}$–log$g$ diagram) are slightly different. Moreover, because the initial stellar mass for the secondary RC stars are larger, they are in general younger than the primary RC stars. However, the two types of RC stars are not significantly separated in the $T_{\rm eff}$–log$g$ diagram since no clear gap is found between the two populations. Although they can be separated from their distinct asteroseismic features (Bedding et al., 2011; Stello et al., 2013), only very few stars have accurate seismic measurements. Therefore, we turn to statistically separate the young and old populations of RC stars with the help of the isochrones. We use the PARSEC isochrones (Bressan et al., 2012) for the age separation. The triangles shown in the panels of Figure 2 are the theoretical positions of the helium core burning stars in $T_{\rm eff}$–log$g$ plane with

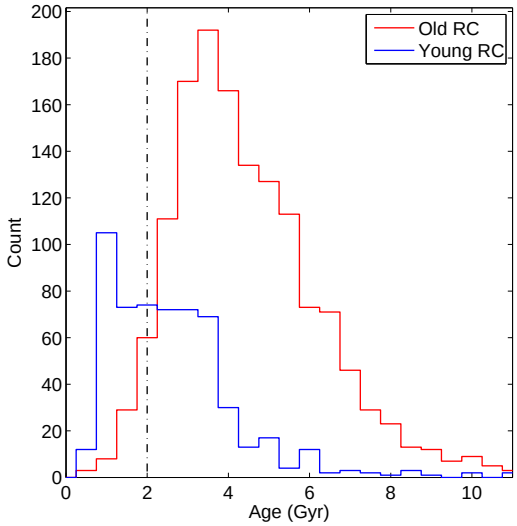

Fig. 3 The distribution of the age for the isochrone-separated young (blue line) and old (red line) RC stars. The age is derived from Martig et al. (2016). The vertical black dot-dashed line indicates the position of 2 Gyr.

different metallicities (from the left to the right panels, [Fe/H]=(-0.6, -0.3), (-0.3,0.0), and (0.0, 0.4), respectively). For each [Fe/H] bin, we select a straight line best fitting the isochrone data points at 2 Gyr as the separation line. We define the RC stars located below the 2 Gyr line to be the young population and those located above the 2 Gyr lines to be old.

Some RC stars younger than 2 Gyr may locate above the separation lines due to the large uncertainty of their log$g$ or because they are very massive ($\gtrsim 10M_{\odot}$) and hence the intrinsic location is above the lines. For the later case, these stars can be negligible because they are very rare. For the former case, we assess the performance of the age separation using the APOGEE data. We cross-match the LAMOST RC catalog with the APOGEE data with age estimates from Martig et al. (2016). We find about 2100 common RC stars after cross-matching. Figure 3 shows the distributions of age for the young (blue line) and old (red line) RC stars identified from Figure 2. We find that most of the old RC stars are located in the right side of the 2 Gyr line (the vertical black dotted-dash line). While lots of the young RC stars are older than 2 Gyr, most of them are younger than the old population. The mean values (standard deviations) of the age are 2.7 (1.6) and 4.6 (2.1) Gyr for the isochrone-identified young and old RC stars, respectively. This shows that the over-simplified isochrone-based age separation is sufficient to separate the young/old populations. Because Martig et al. (2016) did not ross-calibrate their ages with the PARSEC isochrones, the age values in Figure 3 do no necessarily to be consistent with those in Figure 2.

2.3 The final sample

We further select the RC stars close to the Galactic mid-plane with the criterion of $|z| < 1$ kpc, where z is the vertical height above or beneath the mid-plane. To ensure that the stellar parameters applied in the above data selection is reliable, we only select the stars with signal-to-noise ratio larger than 10. Finally, we obtain 62,813 old and 29,118 young RC stars. Figure 4 displays the spatial distributions of the old (in left panels) and young (in the right panels) RC stars in the Galactocentric cylindrical coordinates.

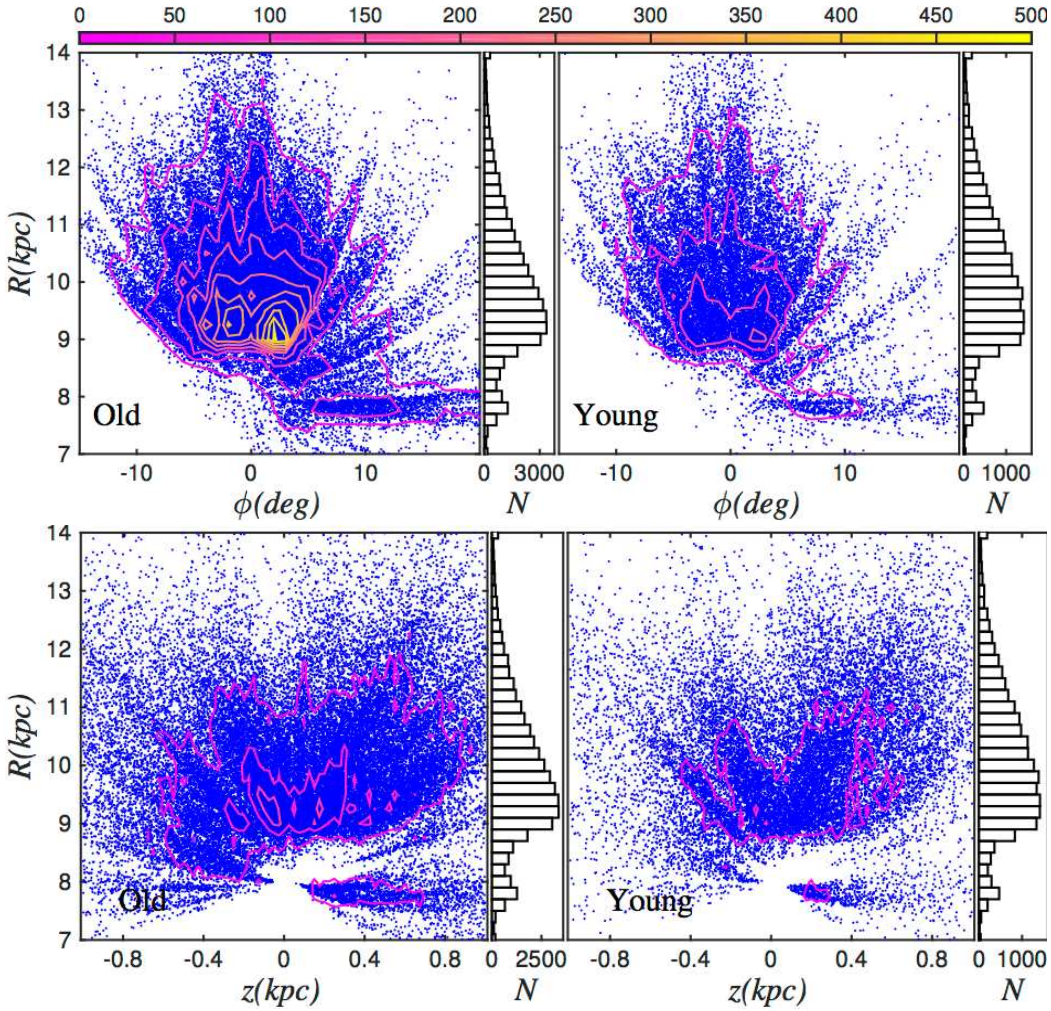

Fig. 4 The spatial density distribution, in Galactic cylindrical coordinates, for the old (left column) and young (right column) RC populations. The color contours represent for the number density of the stars with levels of from 50 to 500 stars per bin with step of 50.

Figure 5 represents the sample distribution in the l vs. b plane. The stars are mainly towards the Galactic anti-centre.

3 METHOD

Ideally, to obtain the in-plane velocity of the Galactic disc, we need to know the tangential velocity as well as the line-of-sight velocity for the tracers. In practice, as shown in Figure 4, lots of the samples are too far to have reliable proper motions. Therefore, we cannot directly obtain the tangential velocities for them. However, we can obtain the $\langle v_R \rangle$, $\langle v_\phi \rangle$, and $\langle v_z \rangle$ at given Galactocentric radius R through velocity de-projection technique.

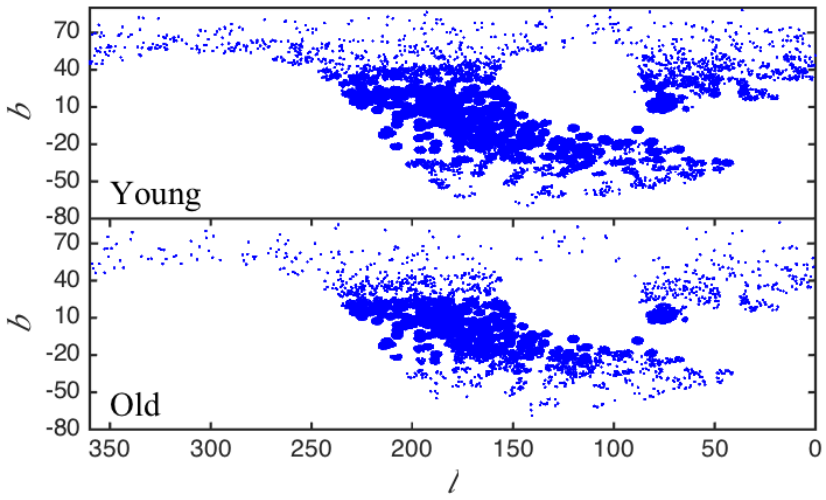

Fig. 5 Distribution of the sample in the l vs. b plane.

3.1 The velocity de-projection approach

Given a star, the line-of-sight velocity can be obtained from

$$v_{los} = -v_R \cos(l+\phi)\cos b \; + \; v_\phi \sin(l+\phi)\cos b \\ + \; v_z \sin b - v_{\odot,los}, \tag{1}$$

where l, b, and ϕ are Galactic longitude, latitude, and azimuth angle with respect to the Galactic center, respectively.

The line-of-sight velocity for the star of interest should follow the underlying distribution function at the position of the star, i.e. (R, ϕ, Z). Then the expectation of the line-of-sight velocity at the position, denoted as $E(v_{los}|R,\phi,z)$, turns out to be

$$E(v_{los}|R,\phi,z) \; = -E(v_R|R,\phi,z)\cos(l+\phi)\cos b \\ +E(v_\phi|R,\phi,z)\sin(l+\phi)\cos b \\ +E(v_z|R,\phi,z)\sin b - v_{\odot,los}. \tag{2}$$

Because of the existence of the bar and spiral arms, the Galactic disc should not be kinematically axisymmetric. Then the three velocity components, v_R, v_ϕ, and v_z should vary with ϕ, although the difference may be small within $\sim 20^\circ$, to which the data samples essentially span in ϕ. Mathematically, we can approximate each term of $E(v.|R,\phi,z)$ through Taylor expansion. Given that the variation of the velocity with ϕ (i.e. the derivative of velocity about ϕ) is small, the averaged value can be obtained by ignoring all the higher order terms than 1 in Taylor expansion and only keep the zero-order term, which is constant about ϕ.

Similarly, because the data samples only cover $|z| < 1$ kpc, we take the zero-order approximation of the three velocities with respect to z and finally obtain

$$E(v_{los}|R,\phi,z) \; \approx -E(v_R|R)\cos(l+\phi)\cos b \\ +E(v_\phi|R)\sin(l+\phi)\cos b \\ +E(v_z|R)\sin b - v_{\odot,los}. \tag{3}$$

Note that Bond et al. (2010) and Smith et al. (2012) found that, in the solar neighbourhood, v_ϕ decreases with Z. Therefore, $E(v_\phi|R)$ should not be the value at $z = 0$, but takes a value between $v_\phi(R, z = 0)$ and $v_\phi(R, z = \pm 1)$, because of the averaging over z.

Moreover, Carlin et al. (2013) showed that $\langle v_R \rangle$ and $\langle v_z \rangle$ also vary with z. Again, such slightly asymmetric motions are ignored in Eq. (3) through the zero-order approximation.

Finally, at a small R bin, the three expected velocity components can be statistically derived from one dimensional v_{los} of a bunch of stars located within the R bin, if only stars in the bin span a large angle, and their v_{los} can provide lots of directions on the sky. In the rest of the paper, we denote the three averaged velocities at R bin as $\langle v_R \rangle$, $\langle v_\phi \rangle$, and $\langle v_z \rangle$. Although the zero-order approximation ignores a lot of the detailed variations of the velocities, the method still can be very useful in investigating the asymmetric motion along R.

The solar motion about the Galactic center projected to the line of sight can be written as

$$v_{\odot,los} = U_\odot \cos l \cos b + (v_0 + V_\odot) \sin l \cos b + W_\odot \sin b, \tag{4}$$

where $U_\odot$, $V_\odot$, and $W_\odot$ are the three components of the solar motion w.r.t the local standard of rest (LSR) and v_0 is the circular speed of the LSR. We adopt the solar motion as $(U_\odot, V_\odot, W_\odot) = (9.58, 10.52, 7.01)\,\mathrm{km\ s^{-1}}$ (Tian et al. , 2015), the distance of the Sun to the Galactic center as $R_0 = 8\,\mathrm{kpc}$, and the circular speed of LSR as $v_0 = 238\,\mathrm{km\ s^{-1}}$ (Schönrich , 2012).

Although McMillan & Binney (2009) found that the de-projection can induce systematic bias in velocity ellipsoid, especially the cross-terms, Tian et al. (2015) have proved that the de-projection approach can well reproduce the first-order momenta, i.e. the mean velocity components, without taking into account the bias due to the spatial sampling.

3.2 Method validation with the mock data

Before we apply the velocity de-projection method to the observed data, we run a Monte Carlo simulation to validate the method using a mock dataset. The mock dataset borrows the 3D spatial positions from the observed RC samples so that it can reflect the same spatial sampling as the survey. The 3D velocities of the mock stars are randomly drawn from a pre-defined velocity distribution function such that we can compare the resulting mean velocities derived from the de-projection method with the pre-defined "true" values. Meanwhile, since we use the same spatial positions for the observed RC stars, the test is also able to derive the uncertainties of the mean velocity components induced by the spatial sampling of the survey.

For each mock star, we draw an arbitrary velocity vector from a 3D Gaussian distribution with the peak value of (v_R, v_ϕ, v_z)=(0, 200, 0) $\mathrm{km\ s^{-1}}$and dispersion of (σ_R, σ_ϕ, σ_z)=(35, 25, 20) $\mathrm{km\ s^{-1}}$. Then, for each R bin we determine the most likely $\langle v_R \rangle$, $\langle v_\phi \rangle$, and $\langle v_z \rangle$ and their uncertainties using the Markov chain Monte Carlo (MCMC) simulation[1]. We repeatedly produce 50 sets of the mock dataset with different random velocities drawn from the same Gaussian distribution and the final mean in-plane velocities as functions of R are shown in Figure 6 for the mock data mimic to the young and old populations, respectively. The top panel shows the mean radial velocity as a function of R for the mimic young (blue asterisks) and old (red circles) mock stars. The de-projection-derived $\langle v_R \rangle$ for both populations well reproduces the true value of $\langle v_R \rangle$, which is zero. The error bars at various R bins are the standard deviations of $\langle v_R \rangle$ for the 50 simulations. The first two points at $R < 8\,\mathrm{kpc}$ show larger errors, because the lines of sights for the stars in these bins are less sensitive to the radial velocity.

The bottom panel shows the test result for the azimuthal velocity. Again, the de-projection-derived $\langle v_\phi \rangle$ well follows the "true" value of $200\,\mathrm{km\ s^{-1}}$. Compared with $\langle v_R \rangle$, the error bars of $\langle v_\phi \rangle$ are slightly larger because the observed RC stars expand in a much smaller range in azimuth angle near the Galactic anti-center direction and thus they are less sensitive to the azimuthal velocity.

Nevertheless, this test illustrates that the velocity de-projection approach is feasible to derive $\langle v_R \rangle$ and $\langle v_\phi \rangle$ with moderate uncertainties due to the spatial sampling of the survey.

[1] We use the *emcee* code to run the MCMC (Foreman-Mackey et al., 2013)

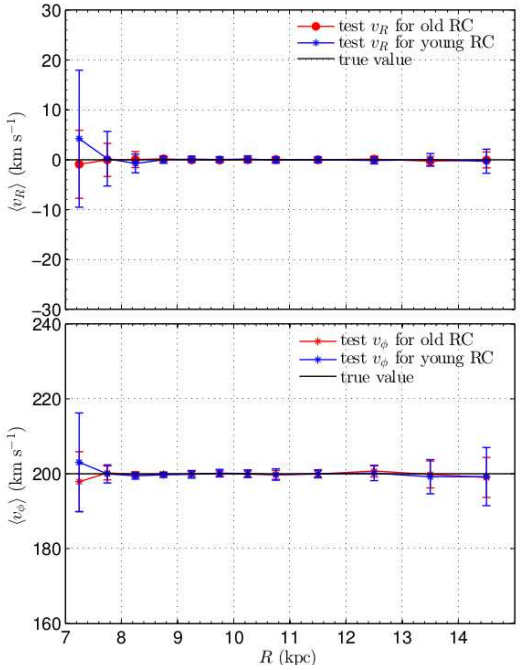

Fig. 6 The mean in-line velocities and their uncertainties derived from the velocity de-projection for the mock data. The top panel shows the variation of $\langle v_R \rangle$ with R and the bottom shows the variation of $\langle v_\phi \rangle$ with R. The red and blue lines are the estimated velocities from mimic old and young RC samples, respectively. The black lines indicate the input values when generating the mock data.

Table 1 The mean in-plane velocities in each R bin for the young and old RC stars.

R	Num. of stars		$\langle v_R \rangle$		$\Delta\langle v_R \rangle$	$\langle v_\phi \rangle$		$\Delta\langle v_\phi \rangle$
kpc			km s^{-1}			km s^{-1}		
	Young	Old	Young	Old	Young - Old	Young	Old	Young - Old
7.75	1617	4882	-11.48 ± 5.66	-6.67 ± 3.72	-5.13 ± 6.77	232.48 ± 2.33	227.08 ± 1.98	5.45 ± 3.06
8.25	2851	7793	-5.11 ± 2.03	-4.20 ± 1.42	-1.29 ± 2.48	233.09 ± 0.66	226.66 ± 0.72	6.99 ± 0.98
8.75	6003	13827	-0.84 ± 0.67	-1.23 ± 0.49	0.09 ± 0.83	226.60 ± 0.58	222.30 ± 0.59	4.29 ± 0.83
9.25	8935	19647	1.27 ± 0.54	1.11 ± 0.43	-0.10 ± 0.69	227.63 ± 0.82	222.35 ± 0.58	5.74 ± 1.00
9.75	8744	18508	4.51 ± 0.51	3.12 ± 0.48	1.18 ± 0.70	223.30 ± 0.91	218.75 ± 0.82	4.67 ± 1.22
10.25	7726	15444	7.09 ± 0.57	4.77 ± 0.46	2.35 ± 0.73	221.41 ± 1.00	217.84 ± 0.93	3.43 ± 1.37
10.75	6403	12588	7.62 ± 0.70	4.54 ± 0.45	3.06 ± 0.83	221.12 ± 1.33	218.90 ± 1.23	1.74 ± 1.81
11.50	4406	8678	8.11 ± 0.64	4.75 ± 0.41	3.29 ± 0.76	227.22 ± 1.03	224.57 ± 0.92	2.20 ± 1.38
12.50	1977	4063	7.77 ± 0.77	5.79 ± 0.49	1.97 ± 0.91	232.54 ± 2.11	231.58 ± 1.85	0.65 ± 2.81
13.50	693	1413	6.63 ± 1.28	5.93 ± 0.98	0.87 ± 1.61	243.40 ± 4.61	236.49 ± 4.09	6.12 ± 6.16
14.50	264	536	6.99 ± 2.49	3.22 ± 1.42	3.77 ± 2.87	241.98 ± 8.11	248.95 ± 5.73	-6.97 ± 9.93

To assess whether the presumption of the 3D Gaussian velocity distribution affects the de-projection, we further run a more realistic test using a torus model-based non-Gaussian velocity distribution. The result of the second test, which is briefly described in Appendix A, shows no significant difference with the first one.

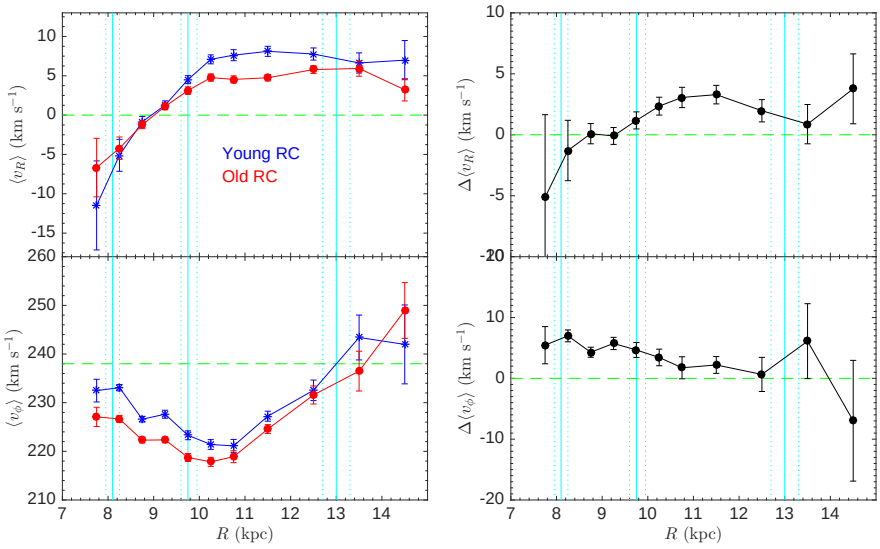

Fig. 7 The top-left panel displays the variation of $\langle v_R \rangle$ for the young (blue) and old (red) RC stars. The green dashed values indicate the zero line. The bottom-left shows the variation of $\langle v_\phi \rangle$ for the both populations. The green dashed line indicates the 238 km s^{-1} as a reference. The top-right panel shows the differential radial velocity (Young - Old) along R. And the bottom-right panel shows the differential azimuthal velocities as a function of R. The cyan vertical solid and dash lines in all panels mark the locations of spiral arms (Reid et al., 2014). The corresponding values in all four panels are also specified in Table 1.

4 RESULTS

Tian et al. (2015) have claimed that the LAMOST line-of-sight velocity is systematically smaller than the APOGEE measure by 5.7 km s^{-1} for unclear reason. Thus, we add 5.7 km s^{-1} to the line-of-sight velocity for all the RC stars before deriving the mean in-plane velocity components.

We then apply the velocity de-projection technique to the observed dataset and obtain the 3D mean velocity components at each R bin, as shown in the left panels of Figure 7. Meanwhile, all the data shown in the plots are also listed in Table 1. In this work, we only focus on the in-plane velocities, i.e. $\langle v_R \rangle$ and $\langle v_\phi \rangle$. It is worthy to note that the velocity de-projection also works out the mean vertical velocity. However, since this work mainly focuses on the particular velocities in the Galactic mid-plane, more investigations on the vertical velocity will be discussed in another work (Liu et al. in preparation).

4.1 Radial variation of $\langle v_R \rangle$

The top-left panel of Figure 7 shows the radial variation of $\langle v_R \rangle$ for both the young (blue lines) and old (red lines) RC stars. The error bars are composed of two parts: the uncertainty of the derived $\langle v_R \rangle$ from the MCMC procedure (the error induced by the method) and the uncertainty of the spatial sampling obtained from the Monte Carlo simulation mentioned in section 3.2 (see Figure 6).

The most prominent feature displayed in the panel is that $\langle v_R \rangle$ is oscillated along R for both populations: $\langle v_R \rangle$ is negative at $R \lesssim 9$ kpc, while it becomes positive beyond $R \sim 9$ kpc.

The overall trend of the radial variation of $\langle v_R \rangle$ for both RC populations is quite consistent with Bovy et al. (2015), who mapped the line-of-sight velocity into X-Y plane using APOGEE RC stars

(see their figure 2). If we only focus in about 1 kpc around the Sun, the variation of the radial velocity with R is also in agreement with Siebert et al. (2011a). At the location of the Sun, their v_R reads about $-7 \sim -24\,\mathrm{km\ s^{-1}}$, while we derive about $-6\,\mathrm{km\ s^{-1}}$ for the young RC stars. We then look at the variation of $\langle v_R \rangle$ from Carlin et al. (2013) and find that at $R \lesssim 9\,\mathrm{kpc}$, their radial velocities are about $-10\,\mathrm{km\ s^{-1}}$ and at $R \gtrsim 9\,\mathrm{kpc}$, their radial velocity increases to about $-5\,\mathrm{km\ s^{-1}}$. The increasing of $\langle v_R \rangle$ with increasing R in their result is similar to this work, while the values of the velocity shift by about $-10\,\mathrm{km\ s^{-1}}$ contrast to our result. Notice that Carlin et al. (2013) measured the radial velocity from the combination of the line-of-sight velocities and the proper motions, complicated systematics may be responsible for the offset. Moreover, Carlin et al. (2013) did not correct the LAMOST DR1 derived line-of-sight velocities by adding $5.7\,\mathrm{km\ s^{-1}}$ for the correction of the systematic offset.

Although the overall trends and the cross-zero points of the radial profile of $\langle v_R \rangle$ for the young and old populations are quite similar, they show difference in amplitude of $\langle v_R \rangle$ at different R. The top-right panel of Figure 7 shows the differential radial velocity derived by subtracting the velocities of the old population from that of the young. At $R < 8\,\mathrm{kpc}$, the radial velocity of the young population is smaller than that of the old by about $5\,\mathrm{km\ s^{-1}}$ with large uncertainty. When $8 < R < 9.5\,\mathrm{kpc}$, the radial velocities of the two populations are roughly the same. However, when $9.5 < R < 13\,\mathrm{pc}$, the radial velocity of the young population is larger than that of the old by at most $3\,\mathrm{km\ s^{-1}}$, and subsequently shows a bump in $\Delta\langle v_R \rangle$ in between $R \sim 9.5$ and 13 kpc. When we superpose the locations of the spiral structures, i.e. the local, Perseus, and Outer arms (Reid et al., 2014), it shows that the bump in $\Delta\langle v_R \rangle$ happens in between the two spiral arms: Perseus and Outer arms.

4.2 Radial variation of $\langle v_\phi \rangle$

The stars are mainly located in the Galactic anti-centre, but still expand a large range in l as shown in Fig. 5, so $\langle v_\phi \rangle$ can be effectively constraint, just not as well as $\langle v_R \rangle$ in Eq. (3). The bottom-left panel of Figure 7 displays the radial profiles of $\langle v_\phi \rangle$ for the young (blue line) and old (red line) RC stars. As a reference, the dashed horizontal line indicates the velocity of $238\,\mathrm{km\ s^{-1}}$, which is the adopted circular speed in the solar neighbourhood.

The radial profile of $\langle v_\phi \rangle$ shows different trend at different radii. In the region of $R \lesssim 10.5\,\mathrm{kpc}$, the mean azimuthal velocities for both the young and old populations mildly decrease by $\sim$10 $\mathrm{km\ s^{-1}}$. Beyond $R \sim 10.5\,\mathrm{kpc}$, the mean azimuthal velocities for both populations increase to 240–245 $\mathrm{km\ s^{-1}}$ at $R \sim 13\,\mathrm{kpc}$. Such a U-shape profile is quite consistent with the result from Liu et al. (2014a), who used the primary RC stars to reconstruct the in-plane kinematics of the Galactic outer disc.

The bottom-right panel of Figure 7 shows the radial profile of the differential mean azimuthal velocities, $\Delta\langle v_\phi \rangle$, which is derived from the subtraction of $\langle v_\phi \rangle$ for the old stars from that for the young stars. It can be seen that $\Delta\langle v_\phi \rangle$ mildly declines from about $5\,\mathrm{km\ s^{-1}}$at $R \sim 8\,\mathrm{kpc}$ to about zero at around 12 kpc.

5 DISCUSSIONS

5.1 The radial profile of the radial velocity

Previous works have shown that the velocity wave perturbed by the spiral structures are always spatially correlated with the spiral arms (Siebert et al., 2012; Faure et al., 2014; Grand et al., 2015). The oscillation in radial velocity, however, does not show such kind of correlation with any spiral arm in the outer disc. On the other hand, the perturbation from the merging dwarf galaxies, e.g. the Sgr dwarf, may raise vertical wave (Gómez et al. , 2013) but may not intensively affect the in-plane velocity. Therefore, the oscillation may neither be induced by the spiral arms nor by the merging dwarf galaxies.

Then we consider whether it is the Galactic bar that induces such a peculiar velocity in the outer disc.

According to previous works, e.g Binney & Tremaine (2008) and Dehnen (2000), the stellar orbits are different inside and outside OLR when the perturbation of the rotating bar is taken into account.

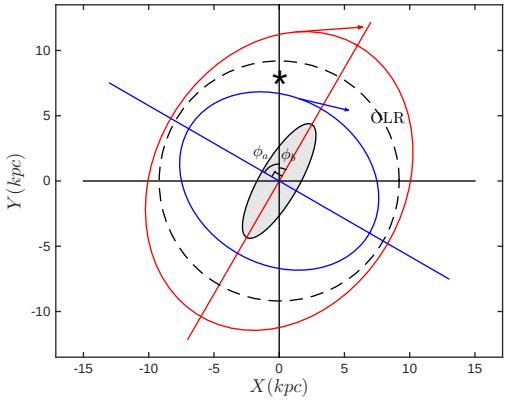

Fig. 8 This cartoon demonstrates the two different stellar orbits inside (blue curve) and outside (red curve) OLR. The red and blue straight lines represent for the major axes of the two orbits, respectively. The arrows indicate the velocity vectors at the Galactic anti-centre direction. ϕ_b is the angle of the bar from the Galactic center-Sun baseline, while ϕ_a is angle of the minor axis of the bar. The location of OLR and the Sun are marked as the black dash circle and asterisk, respectively.

Within OLR the major-axis of the stellar orbits aligns with the minor-axis of the bar, while it aligns with the major-axis when it is located outside OLR. Notice that our samples are roughly concentrated in the Galactic anti-centre direction with a moderate expansion in azimuth direction, then the specific angle from the major-axis of the bar to the Galactic centre (GC)-Sun radial line leads to none-zero radial velocity for these two types of orbits. For the one within OLR, the velocity component projected to the Galactic-anti-centre direction (i.e. the radial velocity) may show negative value, while for the one outside OLR, the radial velocity will show positive value. The cartoon in Figure 8 demonstrates that the radial velocity projected to the GC-Sun line is negative within OLR is negative and positive outside OLR.

At around OLR, where both of the two types of orbits overlap, the negative and positive radial velocities of the different orbits may be canceled with each other at some radius, and consequently, show a zero radial velocity.

Therefore, the radius of the cross-zero point should be quite close to the OLR of the Galactic bar. However, because the samples used in this work are not extremely cold and the contribution to the cross-zero point from the inner and outer disc orbits may be related to the distribution of the disc populations and selection effect of the LAMOST survey, it is not trivial to infer the accurate position of the OLR from this point. Then, we can only give a coarse approximation of the OLR using the cross-zero radius, which is around 9 kpc. This is consistent with the result of López-Corredoira & González-Fernández (2016). They found the average Galactocentric radial velocity is a linear function of R in the range of $5 < R < 16$ kpc, and measured a cross-zero radius of 8.8 ± 2.7 kpc using around 3 000 APOGEE red clump giants.

According to Binney & Tremaine (2008), at OLR we have

$$(\Omega - \Omega_p) = -\frac{\kappa}{2}, \tag{5}$$

where Ω and κ is the azimuthal and radial frequencies, respectively. For the orbits with very low eccentricity, the epicyclic approximation gives

$$\kappa^2 = (R\frac{d\Omega^2}{dR} + 4\Omega^2). \tag{6}$$

The first term turns out to be $-2\Omega^2$ when the circular speed is flat. Then we obtain $\kappa = \sqrt{2}\Omega$. Bring this back to Eq. (5), the pattern speed can be written as $\Omega_b = (1+\sqrt{2}/2)\Omega$. It is worthwhile to point out that the approximation is only valid when the stellar orbits are near-circular so that they can be separated as two harmonic oscillations in azimuthal and radial directions, respectively. Adopting that the circular speed is 238 km s^{-1} and R_{OLR} is $\sim$ 9 kpc, we obtain that the pattern speed of the bar should be around 45 km s^{-1}kpc^{-1}. Alternatively, if the circular speed of 220 km s^{-1} is chosen, the patten speed becomes 42 km s^{-1}kpc^{-1}. This approximation is quite comparable with previous estimations (Gerhard, 2011; Long et al., 2013; Wang et al., 2013). It is noted that Pérez-Villegas et al. (2017) compare the Hercules stream with their dynamical model and found that when the model adopts the pattern speed of 39 km s^{-1}kpc^{-1} for the bar, the Hercules stream-like velocity distribution can be well reproduced from their model. Although the cross-zero radius may not accurately echo the location of the OLR, our estimate of the pattern speed is still quite close to their preferred value.

5.2 The radial profile of the azimuthal velocity

Unlike the radial velocity, the U-shape of the profile of azimuthal velocity shown in the bottom-left panel of Figure 7 is more complicated to be explained. First, the perturbation induced by the bar may not produce any peak or dip in $\langle v_\phi \rangle$ at around OLR if the amplitude of the in-plane velocity is roughly flat at the both sides of OLR. Second, reminding that the derived $\langle v_\phi \rangle$ using the de-projection method is averaged over z, different vertical gradients of v_ϕ at different R may alter the radial profile of $\langle v_\phi \rangle$. Third, v_ϕ highly depends on the orbital angular momentum, whose variation with R in the Galactic outer disc is not clear. Finally, if the outer disk is lopsided (Rix & Zaritsky, 1995), and the Galactic anti-center direction happens to point to the near end of the lopsidedness, then $\langle v_\phi \rangle$ could also show large values. For these reasons, we can not give any clear explanations about the interesting U-shape profile of $\langle v_\phi \rangle$. It would be quite interesting if, in future, one can compare the radial profiles of v_ϕ at different azimuth angles.

5.3 The radial profiles of the differential radial and azimuthal velocities

The roughly same cross-zero points for the young and old populations imply that the two populations respond to the perturbation induced by the bar in a similar way. Normally, one would expect that the younger population, which is also kinematically colder, should be more sensitive to the perturbation. Indeed, the non-zero differential $\langle v_R \rangle$ does show that the amplitude of the non-axisymmetric radial motion for the younger population is larger than the older one by about 3 km s^{-1}.

However, at $R \sim 13.5$ kpc $\Delta\langle v_R \rangle$ decreases to around zero. Such a dip may be related to the Outer arm. But the relatively larger error bar at $R > 13$ kpc implies that the statistics may not be quite robust. Further investigation with more data samples and thus smaller error bar and better spatial resolution is required.

In the bottom-right panel of Figure 7, $\Delta\langle v_\phi \rangle$show a declining trend with R. This is likely because the angular momenta of both the younger and older populations tend to be similar in outer disc.

6 CONCLUSIONS

In this work, we develop a novel method to purify the LAMOST red clump stars and separate them into two groups with different ages. Wan et al. (2015) released a sample of red clump stars from LAMOST, but the sample is contaminated by RGB stars in a small fraction. Through building the [Fe/H]-Mg$_b$ density map, red clump sample is purified up to 97%, and the RGB contamination is reduced by only $\sim$

2%. Because of the different evolutionary tracks, the positions for the two types of stars in the $T_{\rm eff}$-log$g$ diagram are slightly different. With the help of the isochrones, we separate the RC stars into young ($<$ 2 Gyr) and old ($>$ 2 Gyr) groups within the different metallicity bins.

Then, with the de-projection approach, we present the peculiar in-plane velocities derived from the LAMOST red clump stars with different ages. From the variations of the in-plane velocities with the Galactocentric radius for the young and old populations, we discover that: 1) both red clump populations show that the radial velocity is negative within $R \sim 9$ kpc and positive beyond; 2) the young red clump stars show larger mean radial velocity than the old population by about 3 km s^{-1} between $R \sim 9$ and 12 kpc; 3) the radial profile of $\langle v_\phi \rangle$ displays a U-shape in outer disc; and 4) the younger population shows larger mean azimuthal velocity than the older one by about 5 km s^{-1} at $R \sim 8$ and then its $\langle v_\phi \rangle$ gradually decreases with R and shows similar values with the older population at $R \sim 12$ kpc.

The perturbation induced by the bar may be the possible explanation of the oscillation of the radial velocity for both populations. The differential velocities between the younger and older populations may be related to the difference extents of response to the oscillation in the two populations.

The U-shape profile of $\langle v_\phi \rangle$ is extremely interesting without any sensible explanation in this work. We propose to further investigate this issue by looking at the radial profile of the azimuthal velocity at different ϕ in future.

Acknowledgements We thank Robert Grand for the helpful comments. This work is supported by the Strategic Priority Research Program "The Emergence of Cosmological Structures" of the Chinese Academy of Sciences, Grant No. XDB09000000 and the National Key Basic Research Program of China 2014CB845700. H.-J.T acknowledges the National Natural Science Foundation of China (NSFC) under grants 11503012 and U1331202. C. L. acknowledges the NSFC under grants 11373032 and 11333003. Y.-G. W. acknowledges the NSFC grant 11390372 and 11633004. Y. W. acknowledges NSFC under grant 11403056. Guoshoujing Telescope (the Large Sky Area Multi-Object Fiber Spectroscopic Telescope LAMOST) is a National Major Scientific Project built by the Chinese Academy of Sciences. Funding for the project has been provided by the National Development and Reform Commission. LAMOST is operated and managed by the National Astronomical Observatories, Chinese Academy of Sciences.

References

Alam, S., Albareti, F. D., Allende Prieto, C., et al. 2015, ApJS, 219, 12
Bedding, T. R., Mosser, B., Huber, D., et al. 2011, Nature, 471, 608
Binney, J., & Tremaine, S. 2008, Galactic Dynamics: Second Edition, ISBN 978-0-691-13026-2 (HB). Published by Princeton University Press, Princeton, NJ USA, 2008
Binney J., 2012, MNRAS, 426, 1328
Bond, N. A., Ivezić, Ž., Sesar, B., et al. 2010, ApJ, 716, 1
Bovy, J., Bird, J. C., García Pérez, A. E., et al. 2015, ApJ, 800, 83
Bressan, A., Marigo, P., Girardi, L., et al. 2012, MNRAS, 427, 127
Carlin, J. L., DeLaunay, J., Newberg, H. J., et al. 2013, ApJ, 777, L5
Cui, X.-Q., Zhao, Y.-H., Chu, Y.-Q., et al. 2012, Research in Astronomy and Astrophysics, 12, 1197
Contopoulos G., Papayannopoulos T., 1980, A&A, 92, 33
Debattista, V. P. 2014, MNRAS, 443, L1
Dehnen W., 2000, AJ, 119, 800
Deng, L.-C., Newberg, H. J., Liu, C. et al. 2012, Research in Astronomy and Astrophysics, 12, 735
Faure, C., Siebert, A., & Famaey, B. 2014, MNRAS, 440, 2564
Foreman-Mackey, D., Hogg, D. W., Lang, D., & Goodman, J. 2013, PASP, 125, 306
Gerhard, O. 2011, Memorie della Societa Astronomica Italiana Supplementi, 18, 185
Gómez, F. A., Minchev, I., O'Shea, B. W., et al. 2013, MNRAS, 429, 159
Grand, R. J. J., Bovy, J., Kawata, D., et al. 2015, MNRAS, 453, 1867
Kuijken, K., & Tremaine, S. 1994, ApJ, 421, 178

Long, R. J., Mao, S., Shen, J., & Wang, Y. 2013, MNRAS, 428, 3478
Liu, C., van de Ven, G., Fang, M., et al. 2014, Setting the scene for Gaia and LAMOST, 298, 424
Liu, C., Deng, L.-C., Carlin, J. L., et al. 2014, ApJ, 790, 110
Liu, C., Cui, W.-Y., Zhang, B., et al. 2015, Research in Astronomy and Astrophysics, 15, 1137
Liu, C., Fang, M., Wu, Y., et al. 2015, ApJ, 807, 4
López-Corredoira, M. & González-Fernández, C. 2016, ApJ, 151, 165
Martig, M., Fouesneau, M., Rix, H.-W., et al. 2016, MNRAS, 456, 3655
McMillan, P. J., & Binney, J. J. 2009, MNRAS, 400, L103
Pérez-Villegas A., Portail M., Wegg C., Gerhard O., 2017, ApJ, 840, L2
Reid, M. J., Menten, K. M., Brunthaler, A., et al. 2014, ApJ, 783, 130
Rix, H.-W., & Zaritsky, D. 1995, ApJ, 447, 82
Schönrich, R., 2012, MNRAS, 427, 274
Siebert, A., Famaey, B., Minchev, I., et al. 2011, MNRAS, 412, 2026
Siebert, A., Williams, M. E. K., Siviero, A., et al. 2011, AJ, 141, 187
Siebert, A., Famaey, B., Binney, J., et al. 2012, MNRAS, 425, 2335
Smith, M. C., Whiteoak, S. H. & Evans, N. W., 2012, ApJ, 746, 181
Stello, D., Huber, D., Bedding, T. R., et al. 2013, ApJ, 765, L41
Sun, N.-C., Liu, X.-W., Huang, Y., et al. 2015, Research in Astronomy and Astrophysics, 15, 1342
Tian, H. J., Liu, C, Carlin, J. L., et al. 2015, ApJ, 809, 145
Wan, J.-C., Liu, C., Deng, L.-C., et al. 2015, Research in Astronomy and Astrophysics, 15, 1166
Wang, Y., Mao, S., Long, R. J., & Shen, J. 2013, MNRAS, 435, 3437
Widrow, L. M., Gardner, S., Yanny, B., Dodelson, S., & Chen, H.-Y. 2012, ApJ, 750, L41
Williams, M. E. K., Steinmetz, M., Binney, J., et al. 2013, MNRAS, 436, 101
Worthey, G., Faber, S. M., Gonzalez, J. J., & Burstein, D. 1994, ApJS, 94, 687
Wu, Y., Du, B., et al. 2014, IAUS, 306, 340W
Xu, Y., Newberg, H. J., Carlin, J. L., et al. 2015, ApJ, 801, 105
Yao S., et al., 2012, RAA, 12, 772
Zhao, G., Zhao, Y. H., Chu, Y. Q., et al. 2012, RAA, 12, 723

Appendix A: VALIDATION OF THE MODEL WITH NON-GAUSSIAN VELOCITY DISTRIBUTION

It is well known that the velocity distribution, especially the azimuthal component, is not Gaussian in the disc. In order to give more robust test of the velocity de-projection method, we consider a set of mock stars with more realistic non-Gaussian velocity distribution. We first generate the three dimensional velocity distribution at the bins with $R = 8.5, 9.5, \ldots, 13.5$ kpc and $z = -0.75, -0.25, +0.25$, and $+0.75$ kpc (see Figure A.1) based on the torus model from Binney (2012). Given the spatial position of each star in our samples, we randomly draw the three velocity components from the nearest velocity distribution. We draw 50 datasets and calculate $\langle v_R \rangle$ and $\langle v_\phi \rangle$ directly from the three velocity components and show them with red lines in Figure A.2. Then we run the velocity de-projection method to derive $\langle v_R \rangle$ and $\langle v_\phi \rangle$ from the mock line-of-sight velocities. The derived results for the 50 simulations are shown as black lines in Figure A.2. It is seen that there is no significant systematic bias between the de-projection derived velocities and the direct-computed ones, except for $\langle v_R \rangle$ at $R \sim 8$ kpc, at which the derived $\langle v_R \rangle$ is larger by about 0.5 km s^{-1}. Such a systematics would not affect our final result.

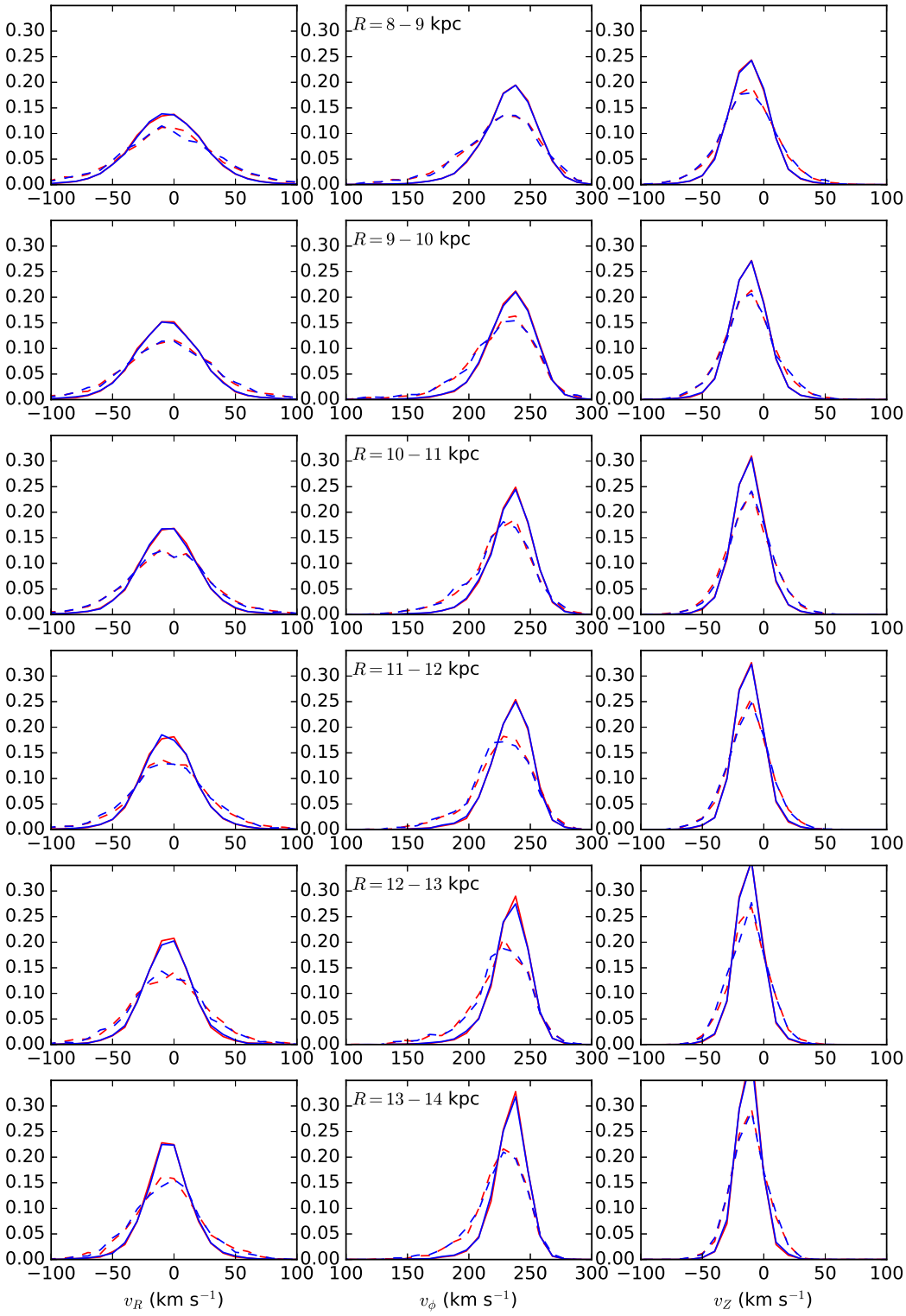

Fig. A.1 The velocity distributions at the spatial bins with $R = 8.5, 9.5, \ldots, 13.5$ kpc and $z = -0.75$, -0.25, $+0.25$, and $+0.75$ kpc. The left, middle, and right columns show the distributions of v_R, v_ϕ, and v_z, respectively. From top to bottom rows are $R = 8 - 9$, $9 - 10$, $\ldots$, $13 - 14$ kpc, respectively. In each panel, the dashed blue, solid blue, solid red, and dashed red represent for $z = -0.75$, -0.25, $+0.25$, and $+0.75$ kpc.

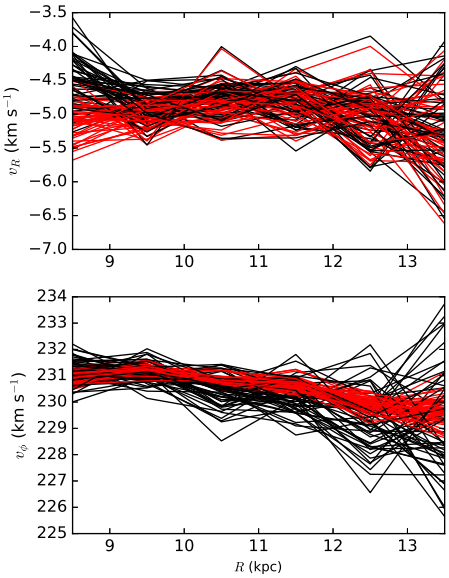

Fig. A.2 The de-projected v_R (top panel) and v_ϕ (bottom panel) derived from line-of-sight velocities of the 50 sets of mock stars are displayed with black lines. The directly computed $\langle v_R \rangle$ and $\langle v_\phi \rangle$ for the 50 sets of mock stars are displayed with red lines.